Engineering Geology 245 (2018) 153–168

Contents lists available at ScienceDirect

Engineering Geology

journal homepage: www.elsevier.com/locate/enggeo

Seismic stability of a rock slope with discontinuities under rapid water drawdown and earthquakes in large-scale shaking table tests

Danqing Song, Ailan Che*, Zhu Chen, Xiurun Ge

School of Naval Architecture, Ocean and Civil Engineering, Shanghai Jiao Tong University, 800 Dongchuan-Road, Shanghai 200040, China

ARTICLE INFO

Keywords:
Rock slope
Discontinuities
Dynamic stability
Rapid water drawdown
Earthquake
Shaking table tests

ABSTRACT

A series of large-scale shaking table tests was performed to clarify the dynamic stability of a rock slope with discontinuous structural surfaces under rapid water drawdown. A wave absorber consisting of a porous sponge and iron gauze was used to eliminate the adverse effects of water waves in the tests. The results show that the slope surface, elevation, surface microtopography, and bedding structural surface have an impact on the amplification effect of the slope. M_{PGA} (the acceleration amplification coefficient) has a positive correlation with the peak acceleration of the input wave. The damage evolution process of the slope during earthquakes can be identified and includes three stages: formation of tiny cracks (0.074–0.148 g), crack propagation in the surface slope (0.148–0.297 g), and sliding failure (0.297–0.446 g). According to the acceleration vectors of the blocks, the differences in the acceleration vectors between adjacent blocks were the main trigger of the slope deformation during earthquakes. P- and S-waves mainly induced the uneven settlement deformation and horizontal sliding movement of the surface slope under the horizontal and vertical seismic loads, respectively. According to the analysis of ΔM_{PGA} (the increment of M_{PGA}) after rapid drawdown occurred, rapid drawdown mainly has a considerable impact on the surface slope between the high and low water levels during earthquakes, particularly from 0.148 to 0.297 g; however, its impact began to decrease after the occurrence of failure deformation from 0.297 to 0.446 g. Moreover, the relationship between the structural surface and the dynamic failure mode was identified.

1. Introduction

Western China is an earthquake-prone region, and the seismic belt is distributed in the Yunnan-Kweichow Plateau (Liu et al., 2013; Zhou et al., 2017). Strong earthquakes and reservoir water level fluctuations are the two primary triggering factors for landslides in Southwest China (Liu et al., 2013; Zhou et al., 2017); in particular, the earthquake-induced landslides cause destructive damage (Wang et al., 2009; Huang et al., 2013). On 12 May 2008, the Wenchuan earthquake occurred in the Longmenshan tectonic zone in Sichuan Province, Southwest China (Wasowski et al., 2011; Fan et al., 2016). The earthquake triggered approximately 56,000 landslides and rock falls (Dai et al., 2011; Huang et al., 2013). According to field surveys of geological disasters, wave propagation has a great impact on the slope stability (Yin, 2008; Wang et al., 2009). Most of the landslides near the epicenter of the earthquake were subjected to strong lateral S-wave forces (Che et al., 2016). Numerous heavy stones were transported from the slopes by the S-waves during the earthquake (Yin, 2008). Therefore, special attention should be paid to the effects of wave propagation on the dynamic stability of rock slopes.

Wave propagation through discontinuous rock masses is governed by the mechanical properties and geometrical distribution of the fracture systems (Huang et al., 2015; Che et al., 2016). Numerous joints are widely distributed in rock slopes under geological stress and consist of weak structural surfaces, resulting in damage to the rock mass integrity (Jiang et al., 2013; Zhou et al., 2017). Moreover, layered rock slopes usually include dominant structural surfaces and numerous orthogonal secondary joints (Xu and Yan, 2014). The distribution of joints is much more complex, due to their uncertain geometric and mechanical parameters, such as azimuthal direction, dip angle and location (Jiang et al., 2013). The failure modes of rock slopes mainly include wedge sliding, plane sliding, toppling or some combination of these modes (Goodman, 1989), but their failure modes also have a close relationship with the distribution of discontinuities in the rock masses (Ghiassi, 1998; Jiang et al., 2013). Given the abovementioned analysis, the dynamic stability of a rock slope with discontinuities becomes very complicated under seismic loading (Dong et al., 2015). In addition, reservoir water level fluctuation has an impact on the stability of landslides (Berilgen, 2007;

* Corresponding author.
E-mail address: alche@sjtu.edu.cn (A. Che).

https://doi.org/10.1016/j.enggeo.2018.08.011
Received 20 February 2018; Received in revised form 24 July 2018; Accepted 19 August 2018
Available online 22 August 2018

Shao et al., 2016; Gao et al., 2014; Song et al., 2017b). In particular, reservoir water drawdown is a key triggering factor of reservoir landslides (Xia et al., 2013; Gao et al., 2014; Moregenstern, 2015). More importantly, if an earthquake occurs during rapid water drawdown, the dynamic stability of reservoir landslides will be more complicated under the combined action of the two triggers, particularly for the rock slopes with complex geological structures. Therefore, special attention should be paid to the dynamic stability of rock slopes under rapid drawdown during earthquakes.

The acceleration response of rock slopes is the basic information and core parameter for evaluating their seismic dynamic response (Song et al., 2017a). Many researchers have studied the dynamic response of rock slopes according to the analysis of peak ground acceleration (PGA) by using shaking table tests (Liu et al., 2013; Liu et al., 2014; Gischig et al., 2015). Huang et al. (2013) investigated the dynamic response of an anti-dip landslide triggered by the Wenchuan earthquake and its failure mechanism. Chen et al. (2016) investigated the effect of a weak intercalation on the dynamic response of rock slopes. Fan et al. (2016) investigated the dynamic response of bedding and toppling rock slopes. Che et al. (2016) investigated the dynamic response characteristics of a rock slope with bedding discontinuities. However, different types of geological structures result in different seismic wave transfer routes in rock slopes, thus impacting the amplification effect of the slope (Fan et al., 2016). In particular, there is only a small amount of information on the analysis of the dynamic stability of rock slopes with discontinuities under the combined action of rapid drawdown and earthquakes. However, the large-scale shaking table tests could accurately clarify the dynamic stability of rock slopes with discontinuities under the two triggers. In shaking table tests, the model size, ground motion input parameters and waveform can be controlled based on the case studies to enable the slope dynamic responses to be measured accurately (Wang and Lin, 2011; Song et al., 2017a). Shaking table tests have been a reliable and effective research method to simulate the seismic dynamic response of rock slopes and directly reveal their failure modes during earthquakes (Lin and Wang, 2006; Lin et al., 2015).

This work takes an actual engineering project as an example, and a series of large-scale shaking table tests were performed to clarify the dynamic stability of a rock slope with discontinuous bedding and toppling structural surfaces under rapid drawdown and earthquakes. Compared with previous studies, the geological structure of the model slope, the combination of external loads, and the experimental design are much more complicated for this study. A wave absorber and waterproofing measures were adopted to eliminate the adverse effects of water waves in the tests. Accelerometers were installed in the slope to monitor the acceleration. The dynamic response of the slope is closely related to the slope elevation, slope surface, surface microtopography, and structural surfaces. The failure evolution process of the slope under earthquakes and rapid drawdown was clarified, according to the analysis of the M_{PGA}. The dynamic deformation characteristics of the landslide induced by P-waves and S-waves were discussed by analyzing the acceleration vectors of the blocks. In particular, during earthquakes, the impact of rapid water drawdown on the dynamic stability and failure mechanism of the slope were thoroughly studied by using M_{PGA} and ΔM_{PGA}. Moreover, this work also discusses the influence of structural surfaces on the failure process and mode of the slope.

2. Shaking table tests

2.1. Study area

The study area is in the transition zone between the southeast edge of the Tibetan Plateau and the Yunnan-Kweichow Plateau in Yunnan Province, Southwest China. The neotectonic movement is strong in the study area, and several faults pass through the area. The Jinsha River Bridge and a reservoir have been proposed and will be built in the lower reaches of the study area (Fig. 1). In the recent 10 years, about 20 earthquakes occur in Yunnan Province, for example, on August 28st and 31st, 2013, two earthquakes with ms5.1 and ms5.9 occurred on the boundary between Deqing County, Yunnan Province, and Derong County, Sichuan Province (Yang et al., 2015), moreover, on 3 August 2014, the Ludian ms6.5 earthquake sequence in Yunnan Province (Li et al., 2015). The epicenters of the earthquakes are close to the study area. Therefore, special attention should be paid to the stability of reservoir landslides under rapid water drawdown and earthquakes. Taking the Lijiang slope as the research object, the slope is located on the right bank of the Jinsha River, and the average natural gradient of the slope is approximately 40° (Fig. 2). Many toppling joints and weak structural bedding planes have developed in the rock mass. The topography of the Lijiang slope is shown in Fig. 2b, and its geological section is shown in Fig. 2c. The material parameters of the rock mass and discontinuous structural surface are shown in Table 1, according to direct shear tests and uniaxial compression tests.

2.2. Test equipment

Tests using a bi-directional (horizontal and vertical) electric servo shaking table made by Japan Kokusai Corporation were performed in the Key Laboratory of Loess Earthquake Engineering, Gansu Earthquake Administration. The shaking table is 4 m × 6 m, and utilizes a single, horizontal translation degree of freedom. With a maximum load of 25 t, a maximum horizontal acceleration of 1.7 g and a maximum vertical acceleration of 1.2 g can be reached. Regular and irregular waves can be used as input motions, and the effective frequency range is 0.1 to 70 Hz. An experimental tank was developed for the tests, which was designed as a rigid, sealed box with organic glass and carbon steel plates, as shown in Figs. 3 and 4a. The inside of the experimental tank is 2.8 m × 1.4 m × 1.4 m. Moreover, four waterproofing measures were adopted to avoid water leakage during the tests, including using a stainless steel tank, plastic film, glass glue and a plank, as shown in Fig. 4a. The glass glue was used to seal the joints of the model box, and the plank was mainly used to prevent water from spilling out of the model box during the vibrations.

In addition, water fluctuation will produce strong wave reflection in the experimental tank, resulting in a great difference from the wave propagation in an actual infinite field. Water waves will have an adverse impact on the tests results, resulting in the inaccuracy and unreliability of the test results. Therefore, a wave absorber was needed to eliminate the adverse impact of the water waves. In recent years, porous structures have been widely used in coastal areas as dissipating seawalls to attenuate the wave energy and as breakwaters to protect beaches, inlets, and harbors from wave action (Zhu and Chwang, 2001). Many researchers have carried out numerous theoretical and experimental investigations on the phenomenon of wave interaction with porous structures (Twu and Lin, 1991; Twu and Wang, 1994; Zhu and Chwang, 2001), and the research results show that the wave elimination effect of porous structures effectively attenuated the wave energy. In the model tests of marine engineering, various types of wave absorbers with porous structures were designed to eliminate the adverse impact of water waves (Zhu and Chwang, 2001; Zhan et al., 2010; Gyongy et al., 2014). However, there is little information on wave absorbers for shaking table tests. According to the previous studies, porous structures could be considered to produce the wave absorber. Given the abovementioned analysis, a wave absorber consisting of a porous sponge stuffing and porous iron gauze was installed at the end of the experimental tank to eliminate the adverse effects of the water waves, as shown in Figs. 3 and 4c. The porous sponge was used as the filling medium, and the porous iron gauze was used as the skeleton. The porous sponge and iron gauze were used to absorb the S- and P-waves, respectively.

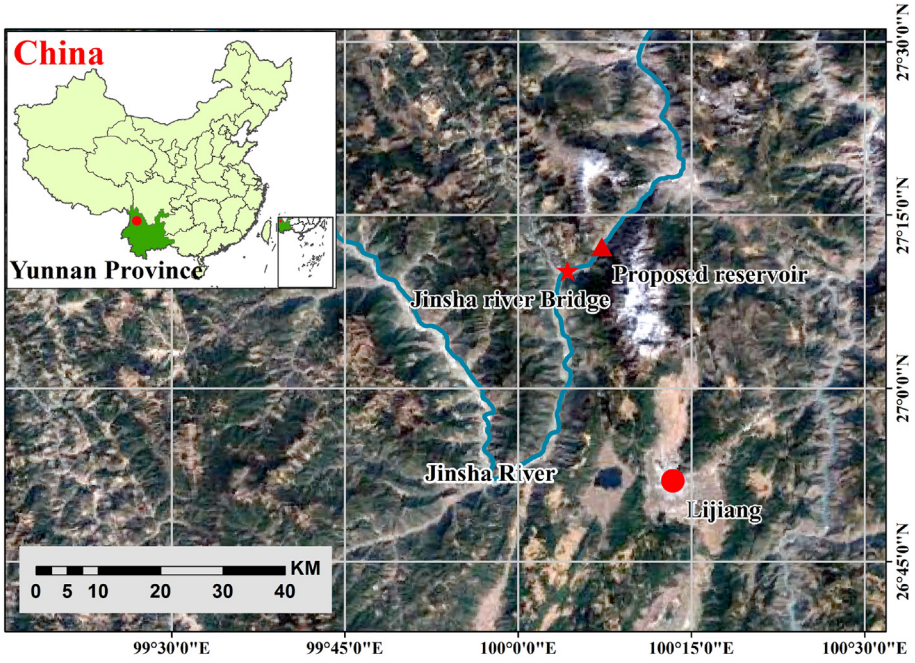

Fig. 1. Location of the study area.

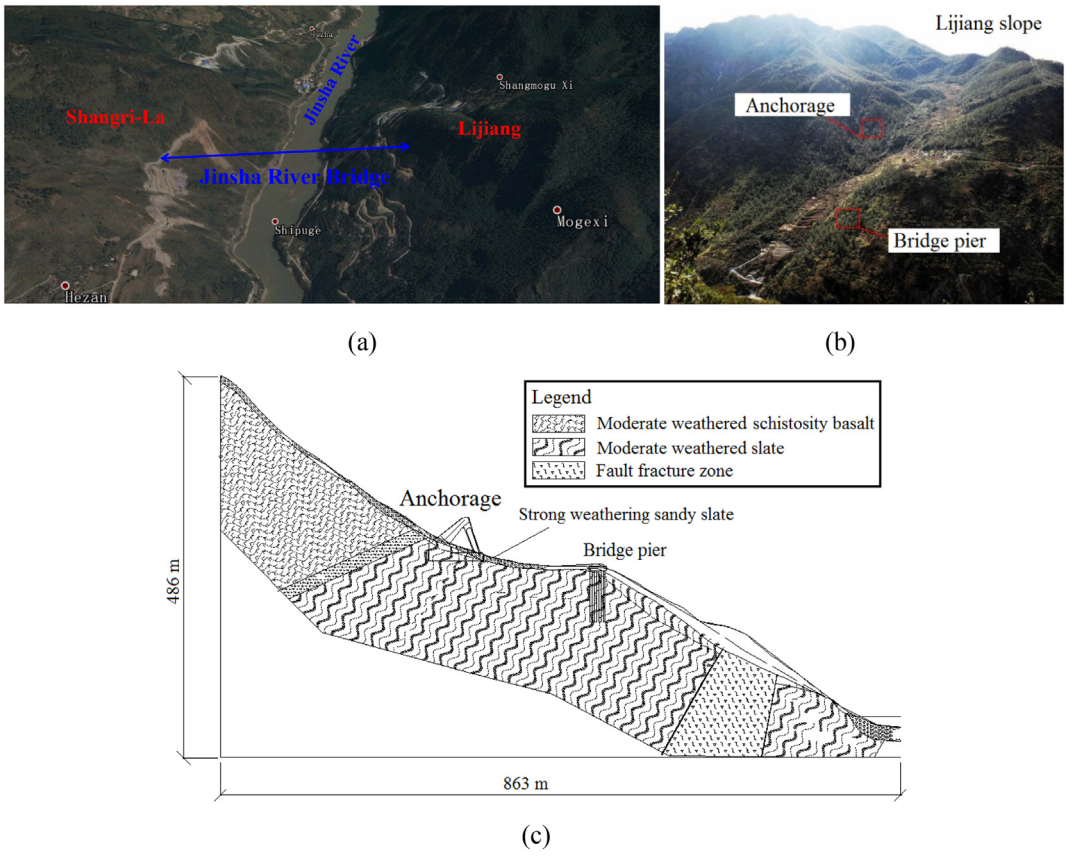

Fig. 2. (a) The topography of project area; (b) the topography of Lijiang slope; (c) the geological section of Lijiang slope.

2.3. Test model

The model slope is simplified based on a geological section of the Lijiang slope (Fig. 2). In the test, the materials and test parameters of the model slope were obtained based on the Buckingham π theorem of similarity. In the present study, seismic acceleration a, mass density ρ, and geometric dimensions L were selected as the controlling parameters, and their scale factors were $C_a = 1$, $C_\rho = 1$, and $C_L = 400$. Based on the controlling quantities, the π terms for the F function and the corresponding scale factors of the other key parameters were calculated and are shown in Table 2. The materials in the model slope were mainly formed of barite, steel slag, sand, plaster, and water at

Table 1
Physico-mechanical parameters of material parameters of the slope.

	Physical and mechanical parameters	Density ρ/kN/m^3	Poisson Ratio μ	Dynamic elastic modulus E/GPa	Friction angle φ (°)	Cohesive force c (kPa)
Lijiang slope	Rock mass	28.5	0.30	10.0	49.0	1920
	Structural surface	/	/	/	36.1	2300
Model slope	Rock mass	28.5	0.3	0.025	49.0	4.8
	Structural surface	/	/	/	36.1	5.75

ratios of 5: 4: 1.3: 2.1, according to a series of triaxial tests. The parameters of the rock masses were listed in Table 1.

The bottom surface of the model slope was 186 × 140 cm in size and 89 cm in elevation. The angles of bedding and toppling structural planes were set 15° and 75° respectively in the model, as shown in Fig. 5. The production process of model is shown in Fig. 7. Different casting times may cause differences in the material characteristics, maintenance difficulties, and inconveniences in the pouring process of the model. These problems will directly influence the accuracy and reliability of the test results. To avoid these problems, the slope model was constructed with prefabricated blocks (Figs. 6 and 7c), which were piled up in four layers. The buffer layer with a thickness of 10 cm was laid on the base of the model to minimize the bottom boundary effect; the buffer layer materials are similar to that of the model (Fig. 7a). In addition, the discontinuous structural surfaces were simulated by gray paperboard, due to the following reasons: According to the Buckingham π theorem of similarity, the thickness of the discontinuous structural plane of the model is < 2 mm, suggesting that its internal friction angle should be simulated accurately, but its cohesive force and thickness can be ignored. Moreover, gray paperboard has some advantages: better stability in water, greater strength, good toughness, longer fibers, greater thickness and greater density. The direct shear experiment results show that the internal friction angle of the gray paperboard is the most similar to those of discontinuous structural planes. Gray paperboard was glued to the surface of the blocks between the two layers, and its position is shown in Fig. 7d.

During the tests, a monitoring system was set up to record the acceleration-time curve. The system includes twenty 3-direction capacitive accelerometers (DH301), which is made by China Donghua Testing Co., LTD., were embedded into the center of the model to reduce the side boundary effect (Fig. 8). Their measurement points embedded at different elevations inside the model slope, as shown in Fig. 5. The frequency range of acceleration sensor is 0–1500 Hz in horizontal and 0–800 Hz in vertical, and its sensitivity is about 66 mV/m·s^{-2} with the measuring range (Peak) being ± 20 m/s^2.

2.4. Input motions

The seismic wave was simulated by inputting acceleration time history curve during the tests. Taking the AS (Artificial synthetic) wave (0.074 g) as an example, its time history and Fourier spectrum are shown in Fig. 9. Two simultaneous loading directions of experimental earthquake excitation (the z and x directions) were applied in the tests. The working conditions of the tests are listed in Table 3, and the experimental process is shown in Fig. 10. Water level drawdown was modeled by setting up high and low water levels. Due to the violent vibration of the experimental tank, and the restriction of the waterproofing measures, the water cannot be quickly released from the experimental tank. Rapid drawdown was modeled by rapidly drawing water out in the shortest possible time, when the shaking table was not moving, rather than during the process of vibration. Additionally, the acceleration data from the test should be preprocessed, primarily by filter and baseline calibration. MATLAB was used to compile the Chebyshev II bandpass filter, in order to filter the wave, and obtain the effective waveform frequency that was mainly in the range of 3–50 Hz.

3. Dynamic acceleration response of the slope during earthquakes

3.1. Dynamic acceleration response

The topographic condition is an important triggering factor of landslides during earthquakes (Geli and Jullien, 1988; Liu et al., 2014). In mountainous areas, the buildings at the top of a slope are more damaged than those located at the base of the slope during earthquakes, manifesting that the surface topography plays an important role in ground motion (Geli and Jullien, 1988). To clarify the influence of topography on the dynamic acceleration response of the slope, the M_{PGA} distributions of the slope under a horizontal seismic load are shown in Fig. 11. M_{PGA} is the ratio of the PGA of the measuring points and PGA of the shaking table surface. Fig. 11 shows that the M_{PGA} increases with the elevation and reaches the maximum at the top of the slope. This phenomenon demonstrates that elevation creates an amplification effect inside the slope and on the slope surface during earthquakes. Furthermore, a sudden increase in M_{PGA} can be observed in Fig. 11 when the elevation reaches the stair-stepping platform, due to a considerable change in gradient near the platform, resulting in a stress concentration phenomenon and an increase in the amplification effect. This phenomenon indicates that slope surface microtopography has an impact on the amplification effect of the slope. In addition, the ratio of the M_{PGA} between the surface slope and the internal slope at the same elevation is shown in Fig. 12, mainly including four different elevations (A6, A7, A10 and A16). Fig. 12 shows that the ratio of M_{PGA} is > 1.0 overall; for example, the ratio of M_{PGA} is mainly from 1.15–1.4 under a horizontal seismic load. Fig. 11 also shows that the M_{PGA} of the slope surface is much larger than that of the internal slope, indicating that the slope surface creates an acceleration amplification effect, and the

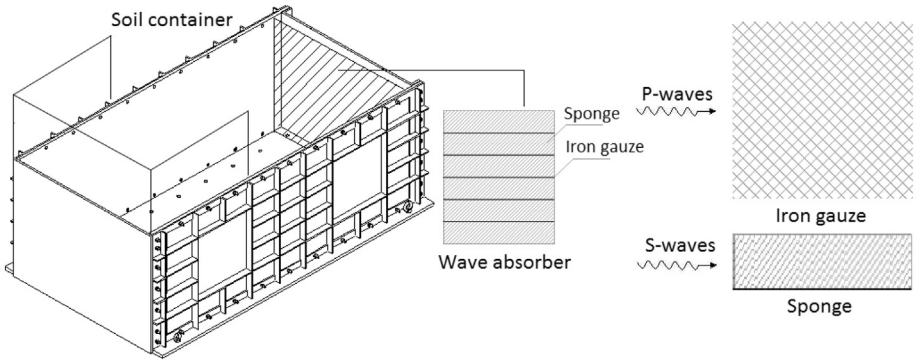

Fig. 3. Experiment tank system.

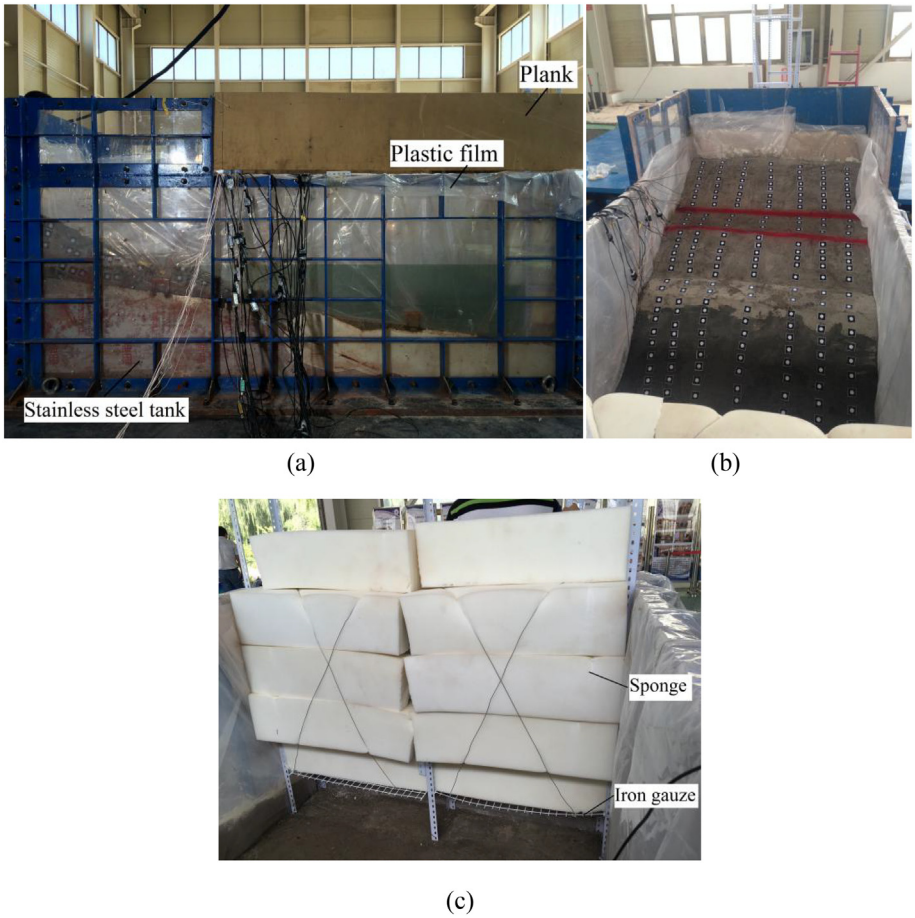

Fig. 4. (a) Experiment tank, (b) scaled model, and **c** wave absorber.

Table 2
The similarity ratios of the test model. Here, L, ρ, and a are controlling parameters.

No.	Parameters	Dimension analysis	Dimensionless (π) item	Similarity ration
1	Density (ρ)	$[M]\ [L]^{-3}$	Controlling parameter	$C_\rho = 1$
2	Physical dimension (L)	$[L]$	Controlling parameter	$C_L = 400$
3	Elasticity modulus (E)	$[M]\ [L]^{-1}[T]^{-2}$	$\pi_E = E/\rho L$	$C_E = C_\rho C_L = 400$
4	Poisson's ratio (μ)	–	1	$C_u = 1$
5	Cohesive force (c)	$[M]\ [L]^{-1}[T]^{-2}$	$\pi_c = c/L$	$C_c = C_L = 400$
6	Internal fraction angle (φ)	–	1	$C_\varphi = 1$
7	Stress (σ)	$[M]\ [L]^{-1}[T]^{-2}$	$\pi_\sigma = \sigma/L$	$C_\sigma = C_L = 400$
8	Strain (ε)	–	1	$C_\varepsilon = 1$
9	Time (t)	$[T]$	1	$C_t = 1$
10	Frequency (ω)	$[T]^{-1}$	$\pi_\omega = \omega/t^{-1}$	$C_\omega = C_t^{-1} = 1$
11	Displacement (s)	$[L]$	$\pi_s = s/\rho La$	$C_s = C_\rho C_L C_a = 400$
12	Velocity (v)	$[L]\ [T]^{-1}$	$\pi_v = v/\rho La$	$C_v = C_\rho C_L C_a = 400$
13	Acceleration (a)	–	Controlling parameter	$C_a = 1$
14	gravitational acceleration (g)	$[L]\ [T]^{-2}$	$\pi_g = g/a$	$C_g = C_a = 1$
15	Damping ration (λ)	–	1	$C_\lambda = 1$

surface slope is the main amplification area. It was found that a large number of rock slopes with weak intercalated layers damaged more severely near the slope surface than inside the slope, during both the 2008 Wenchuan and 2013 Lushan earthquakes in the southwest of China (Dai et al., 2011).

The influence of structural surfaces on the amplification effect of the slope was clarified according to the analysis of M_{PGA} in Fig. 11a. Fig. 11a shows that the M_{PGA} above the bedding structural surface is much larger than that below the structural surface, in particular, above the top structural surface. For example, the M_{PGA} below the structural plane are smaller, approximately < 1.2, 1.24, 1.4, and 1.8 when the peak accelerations are 0.074, 0.148, 0.297, and 0.446 g, respectively. This phenomenon suggests that the bedding structural surface has an amplification effect on the slope. In addition, Fig. 13a shows that the M_{PGA} below the structural surface is smaller and increases linearly with the elevation, overall; however, a sudden increase in M_{PGA} can be observed above the structural surface, inside the slope. Fig. 13b also shows that the M_{PGA} is much smaller below the top structural surface but rapidly increases above the structural surface. Given the above-mentioned analysis, the M_{PGA} has a linear increase below the bedding structural surface but has a sudden increase above the structural surface. This phenomenon suggests that the bedding structural surface has a great amplification effect on a slope, because the transmission and reflection phenomena can be identified when wave propagation occurs through different transmission media (Lee, 2001), directly influencing the acceleration amplification effect of the slope (Fan et al., 2016).

3.2. Dynamic failure evolution process of the slope

The dynamic failure evolution process of the slope under earthquakes was clarified according to the analysis of the M_{PGA}. Fig. 11a shows that the M_{PGA} increases with the increasing peak acceleration of the input wave, suggesting that there is a positive correlation between

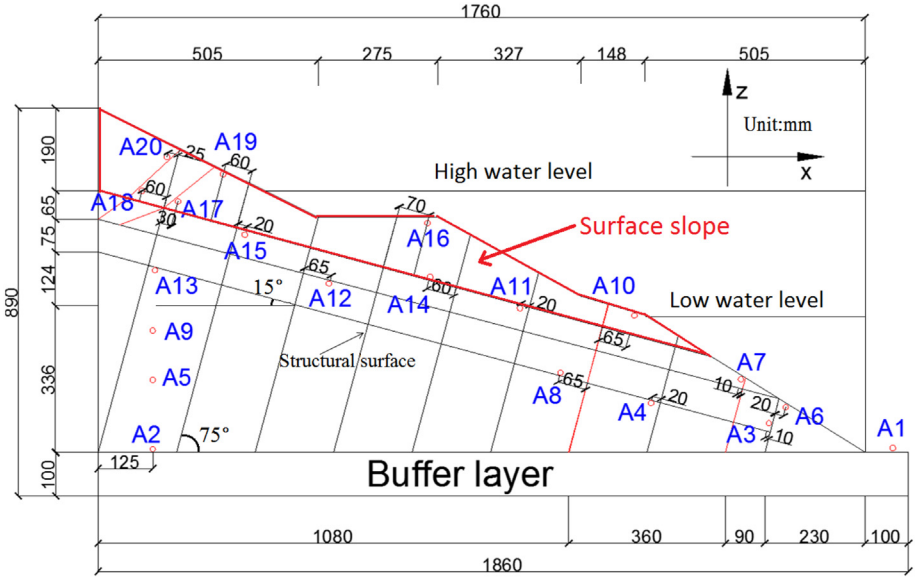

Fig. 5. Cross-sectional illustration of the test model apparatus with discontinuous joints, and showing the layout of monitoring points, and accelerometers.

them; in particular, the M_{PGA} increases rapidly in the surface slope. For example, the M_{PGA} of A20 are approximately 1.49, 1.59, 1.95, and 3.24, when the peak accelerations are 0.074, 0.148, 0.27, and 0.446 g, respectively. This phenomenon suggests that the peak acceleration of the input wave has a great amplification effect on the surface slope. Fig. 14 shows that the M_{PGA} of the internal slope (A2, A5, A6, A7 and A13) increase linearly overall, demonstrating that the internal slope is stable. This result is observed because when waves propagate through rock masses, if no damage occurs inside the slope, the energy transmission of the wave propagation shows a linear relationship with the M_{PGA} of the slope during the process of wave propagation, resulting in the amplification effect changing according to its original trend without large fluctuation.

Moreover, Fig. 14 shows that the M_{PGA} of the surface slope (A10, A16, A18, and A20) increases slowly from 0.074 to 0.148 g, indicating that the slope is stable. The rate of increase in the M_{PGA} further increases from 0.148 to 0.297 g, suggesting that the slope began to undergo damage. It is noteworthy that a sudden increase can be identified from 0.297 to 0.446 g, indicating that large deformation occurs in the surface slope. This is due to an important reason: If any part of the slope suffers dynamic damage as the peak acceleration of the input wave increases, the wave propagation will change considerably and will have a great influence on the dynamic response of the slope. The influence of the energy transmission of the wave propagation on the amplification effect of the slope shows a nonlinear trend during the process of wave propagation. A great change in wave propagation will lead to a dramatic fluctuation or abrupt change in the acceleration amplification effect in the slope structure. Therefore, by analyzing the change rule of the M_{PGA} at different positions in the model slope, the dynamic failure evolution process of the slope during earthquakes can be identified and divided into three stages (Fig. 17): formation of tiny cracks (0.074–0.148 g), crack propagation in the surface slope (0.148–0.297 g), and sliding failure (0.297–0.446 g).

3.3. Dynamic deformation characteristics

To clarify the deformation characteristics of the slope during earthquakes, taking a certain moment as an example, the acceleration vectors of the blocks are shown in Fig. 15. The acceleration vectors of the monitoring points are obtained based on the moment when the acceleration vector at A20 reaches the maximum, but the acceleration vectors of the other points are not maximized. The A/B° in Fig. 15 represents the acceleration/horizontal contained angle, for example, 1.84/261.44° refers to the acceleration and horizontal angle of 1.84 $m{\cdot}s^{-2}$ and 261.44°, respectively.

The blocks movements of the surface slope are not equal but inconsistent during earthquakes. Fig. 15 shows there are differences in the acceleration directions and amplitudes between adjacent blocks, resulting in the differences in the blocks motions, with cracks occurring at the discontinuous joints. Fig. 15a shows that there is a clear difference in the amplitudes and directions of the acceleration vectors between the adjacent blocks under vertical seismic load, resulting in the uneven settlement of blocks. For example, A20 and A19 exhibit 1.88 $m{\cdot}s^{-2}$/78.89° and 1.76 $m{\cdot}s^{-2}$/67.69° when the peak acceleration of the vertical input wave is 0.074 g. Moreover, Fig. 15b shows that the acceleration vectors are also different under a horizontal seismic load,

Fig. 6. Prefabricated blocks production: (a) Block mould; (b) Prefabricated blocks; (c) Gray paperboard; (d) Nonrectangular blocks production.

Fig. 7. The production process of slope: (a) cushion layer; (b) the first layer; (c) the second layer; (d) the laying process of Gray paperboard; (e) the third layer; (f) the fourth layer.

resulting in the occurrence of tensile cracks between adjacent blocks; for example, A16 and A15 exhibit 1.50 $m{\cdot}s^{-2}$/6.23° and 1.69 $m{\cdot}s^{-2}$/345.71°, respectively, when the peak acceleration of the horizontal input wave is 0.074 g. The acceleration amplitude of the front block is greater than that of the back block; for example, A10 (front block) and A11 (back block) exhibit 3.06 $m{\cdot}s^{-2}$/350.89° and 2.77 $m{\cdot}s^{-2}$/359.22°, respectively, when the peak acceleration of the input wave is 0.297 g. In addition, Fig. 15a shows that the acceleration directions of the blocks are close to vertical under a vertical seismic load, suggesting that the P-waves mainly induced settlement under a vertical earthquake loading. Fig. 15b shows that the acceleration directions of the blocks are close to the direction of the consequent structural plane that is a potential slip surface, suggesting that the S-waves mainly induced horizontal sliding movement under a horizontal seismic load. It can also be found that the acceleration vectors under the horizontal seismic load are larger than those under the vertical seismic load, indicating that the S-waves have a greater impact on the deformation of the slope than that of the P-waves.

Given the abovementioned analysis, the differential deformation between adjacent blocks is the main triggering factor of the landslide during earthquakes. The vertical settlement and horizontal slide are the main deformations, which are induced by the P- and S-waves, respectively. The deformation characteristics induced by P- and S-waves during the tests were as follows: P-waves shook the slope vertically, and the differences in the acceleration vectors between adjacent blocks directly trigger uneven settlement deformation, resulting in the occurrence of lateral cracks along toppling structural planes in the surface slope. S-waves shook the slope horizontally and induced longitudinal tension cracks due to the differences in the acceleration vectors

Fig. 8. Acceleration sensor and its placement.

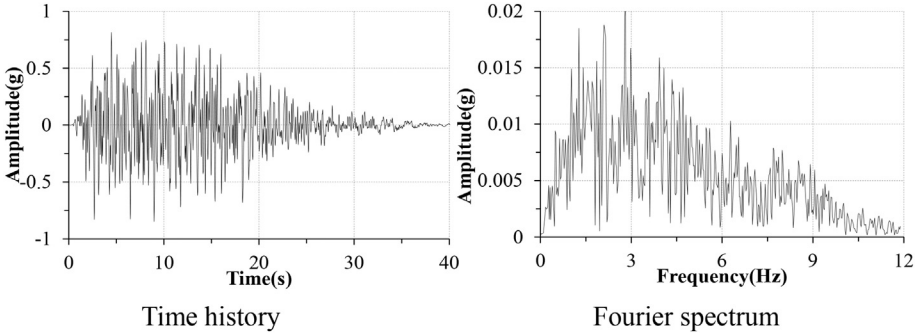

Fig. 9. The input AS wave.

Table 3
The test loading sequence.

Peak amplitude (g)	0.074	0.074	0.148	0.148	0.297	0.297	0.446	0.446
Water level	High	Low	High	Low	High	Low	High	Low
No.	1	2	5	6	9	10	13	14
Vibration direction	*z*	*z*	*z*	*z*	*z*	*z*	*z*	*z*
No.	3	4	7	8	11	12	15	16
Vibration direction	*x*	*x*	*x*	*x*	*x*	*x*	*x*	*x*

between adjacent blocks. S-waves directly induced a larger horizontal shear deformation of the rock slope, resulting in the eventual occurrence of the landslide.

4. Dynamic acceleration response of the slope under rapid water drawdown and earthquakes

4.1. Dynamic failure evolution process of the slope

The dynamic failure evolution process of the slope under rapid drawdown and earthquakes was analyzed in Fig. 16. Fig. 16 shows that the M_{PGA} of the internal slope (A2, A5, A6, A7, and A13) increases linearly overall, indicating that no deformation occurred in the internal slope. However, the M_{PGA} of the surface slope (A10, A16, A18, and A20) increases nonlinearly, suggesting that damage deformation mainly occurs in the surface slope. Moreover, taking A16 and A20 as examples, their M_{PGA} values are shown in Fig. 17. Fig. 17 shows that the dynamic failure evolution process of the slope under the two triggers can be divided into three stages, which is similar to that before rapid drawdown. The rate of increase in M_{PGA} is the largest when the peak acceleration is < 0.148 g after rapid drawdown, with the rate of increase decreases gradually when the peak acceleration is > 0.148 g; in particular, a rapid decrease occurs from 0.297 to 0.446 g. This phenomenon indicates that the slope surface begins to become damaged after rapid drawdown when the peak acceleration is > 0.148 g, and is seriously damaged when the peak acceleration is > 0.297 g. In addition, Fig. 17 shows that both the M_{PGAH} (M_{PGA} before rapid drawdown) and M_{PGAL} (M_{PGA} after rapid drawdown) increase with the peak acceleration of the input wave, but they increase at different rates. The rate of increase in M_{PGAL} decreases gradually with the increasing peak acceleration of the input wave, while the rate of increase in the M_{PGAL} continuously increases. This phenomenon suggests that rapid drawdown has an impact on the change rule of M_{PGA} with the increasing peak acceleration of the input wave because the rapid drawdown further promotes the damage deformation of the slope during earthquakes and weakens the stability of the slope, resulting in the gradual decrease in the rate of increase in M_{PGA}.

Moreover, the damage deformation process of the slope can be identified by either M_{PGAL} or M_{PGAH}. It is notable that a rapid increase in the M_{PGAH} can be identified between damage stages. However, the change in M_{PGAL} is smaller, particularly in the three stages, while M_{PGAL} clearly changes; in particular, a rapid increase in M_{PGAH} can be identified in Stage 3. This indicates that the damage deformation process of the slope can be elucidated by using M_{PGAH}, particularly if a large deformation of the slope occurs, and the rapid increase in M_{PGAH} can reflect the deformation more clearly than M_{PGAL} can.

4.2. Influence of rapid drawdown on the acceleration response during earthquakes

The influence of rapid drawdown on the acceleration response

Fig. 10. (a) During the experiment under reservoir water; (b) high water level.

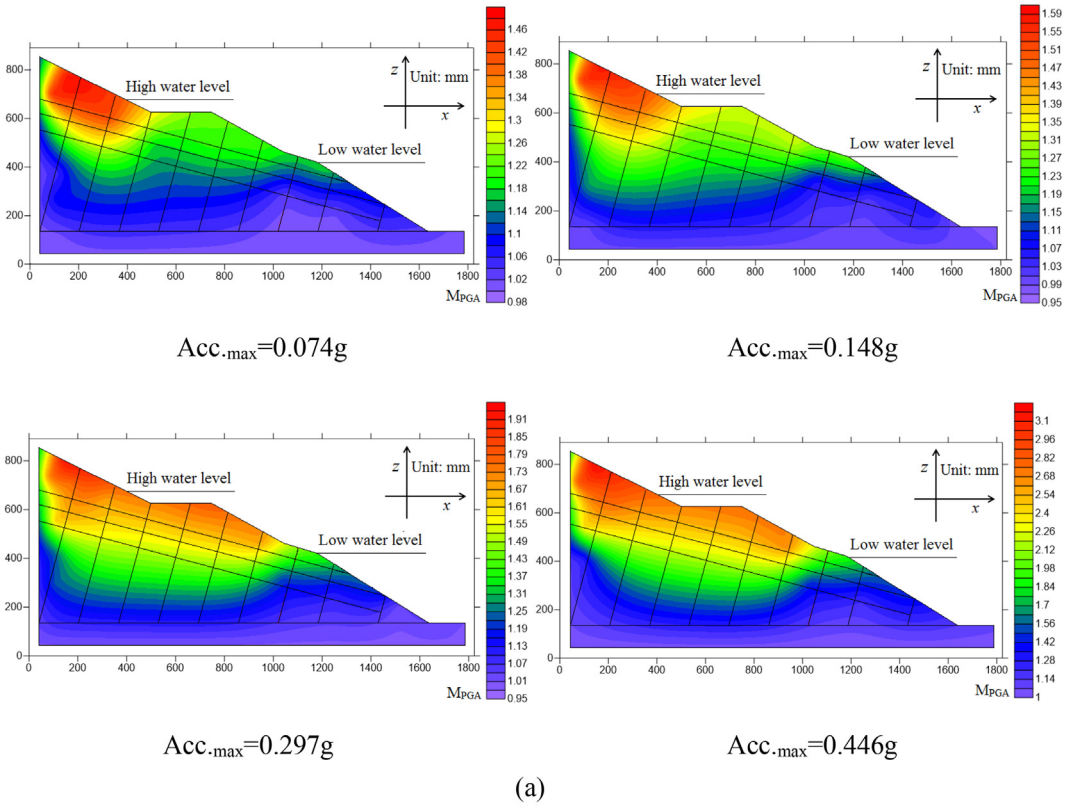

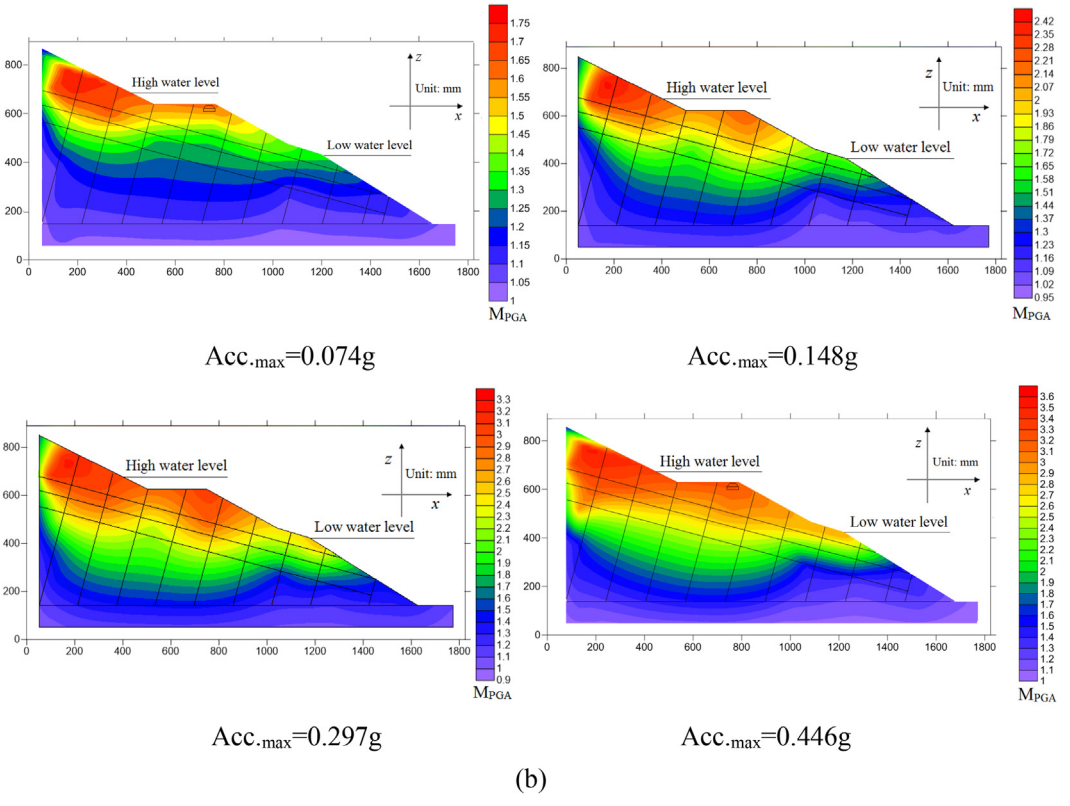

Fig. 11. Distribution of M_{PGA} when input in *x* direction: (a) before rapid drawdown; (b) after rapid drawdown.

during earthquakes was analyzed according to M_{PGA} and ΔM_{PGA}. Fig. 11b shows that M_{PGA} has a certain increase after rapid drawdown. M_{PGAL} is approximately 1.2–1.5 times M_{PGAH} when the peak acceleration is 0.148 g; for example, $M_{PGALmax}$ is approximately 1.55 times $M_{PGAHmax}$, as shown in Table 4. Fig. 11b shows that the distribution of M_{PGAL} is similar to that of M_{PGAH} (Fig. 11a), indicating that rapid drawdown has little impact on the distribution of M_{PGA}. In addition, the distribution of ΔM_{PGA} after rapid drawdown is shown in Fig. 18. Fig. 18 shows that ΔM_{PGA} of the surface slope is much larger than that of the internal slope, in particular, it reaches a maximum between the high

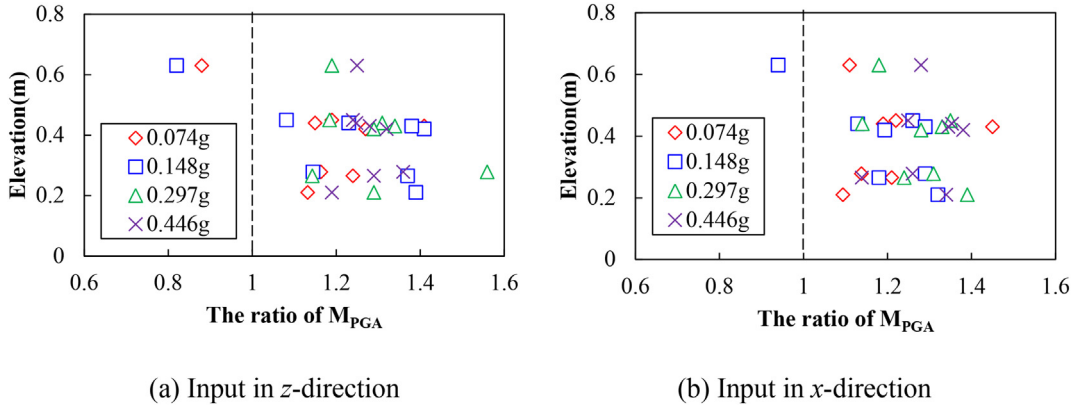

Fig. 12. The ration of M_{PGA} between the internal slope and slope surface under high water level: (a) input in *z*-direction, and (b) input in *x*-direction.

and low water levels. It can be found that rapid drawdown mainly has a great amplification impact on the surface slope between the high and low water levels. This result is observed because during earthquakes, rapid drawdown produces drag force, and the saturation line of the slope descends, and since the slope surface between the high and low water levels is the free surface, this change results in the increase in the amplification effect of the wave propagation in the surface slope.

Moreover, the influence of the two triggers on the amplification effect of the slope was further investigated in Fig. 19. Fig. 19 shows that ΔM_{PGA} of A6 and A7 is smaller in the surface slope, since they are below the low water level, and rapid drawdown has little impact on them. It is worth noting that ΔM_{PGA} undergoes a sudden increase from A7 to A10, indicating that rapid drawdown has a great impact on M_{PGA} above the low water level. For example, ΔM_{PGAmax} is approximately 1.09 between the high and low water levels, but ΔM_{PGA} is < 0.15 below the low water level. ΔM_{PGA} further increases from A10 to A16 and reaches its maximum at A16; however, a decrease in ΔM_{PGA} can be found above A16. This phenomenon suggests that rapid drawdown has a great impact on the amplification effect of the surface slope between the high and low water levels, consistent with the result that the surface slope is seriously damaged between them, as shown in Fig. 21c. In addition, taking three monitoring points of the surface slope as examples, the change rule of ΔM_{PGA} is shown in Fig. 20. Fig. 20a shows that ΔM_{PGA} increases rapidly from 0.074 to 0.148 g under the horizontal seismic load because no apparent damage occurs in the surface slope in this stage. ΔM_{PGA} further increases from 0.148 to 0.297 g, since cracks propagate in the surface slope, resulting in the decrease in the rate of increase of ΔM_{PGA}. However, a sudden decrease in ΔM_{PGA} can be identified from 0.297 to 0.446 g, since large deformation occurs in the surface slope, directly reducing the amplification effect of the slope.

Given the analysis of ΔM_{PGA}, the slope deformation process can also be divided into three stages: the elastic stage (0.074–0.148 g), the plastic stage (0.148–0.297 g), and the failure stage (> 0.297 g). In particular, the plastic stage (0.148–0.297 g) is the cumulative deformation failure stage, and 0.297 g is the critical failure state of the slope. ΔM_{PGAmax} and ΔM_{PGAmin} of the surface slope are approximately 1.09 and 0.65, respectively, at 0.297 g. This result indicates that the failure deformation of the surface slope between the high and low water levels begins in the plastic stage, when ΔM_{PGA} is > 0.65. Moreover, Fig. 20 shows that ΔM_{PGA} under the horizontal seismic load is 1.5–1.8 times that under the vertical seismic load. For example, the ΔM_{PGA} values of A16 are 0.85 and 0.46 at 0.148 g, under horizontal and vertical seismic loads, respectively. It can be found that rapid drawdown has a greater impact on the amplification effect of the slope under S-waves than that under P-waves during earthquakes.

5. Dynamic damage phenomenon and failure mechanism

The structural surfaces in layered rock slopes have a great influence on the dynamic failure modes of the slopes (Zhou et al., 2017). The effects of structural surfaces on the dynamic damage characteristics of the slope during earthquakes were concluded as follows. First, the toppling structural surfaces control the occurrence and development of cracks. Fig. 21a shows that a few tiny cracks initiate in the surface slope along the toppling structural surfaces when the peak acceleration $<$ 0.148 g. When the peak acceleration reaches 0.297 g, many new cracks appear and propagate along the toppling structural surfaces. The cracks further deepen, extend, and coalesce to form penetrating cracks, as shown in Fig. 21b, which further deteriorate the mechanical properties of the rock mass and weaken the slope stability. When the peak acceleration reaches 0.446 g, many penetrating cracks appear along the toppling structural surfaces between the high and low water levels, and serious damage phenomena can be found in the slope surface, as shown in Fig. 21c. Second, the bedding structural surfaces control the formation of the slip surface. Fig. 21c, d show that the topmost bedding structural surface is the main slip surface, since the reservoir water

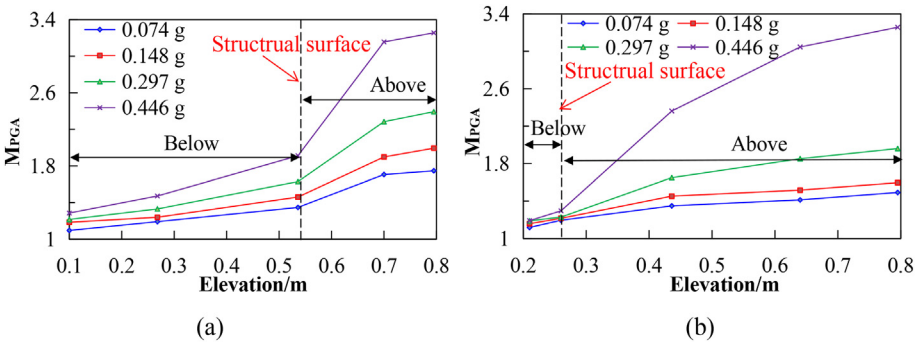

Fig. 13. M_{PGA} change rule when input in *x* direction under high water level: (a) the inside of the slope body; (b) near the slope surface.

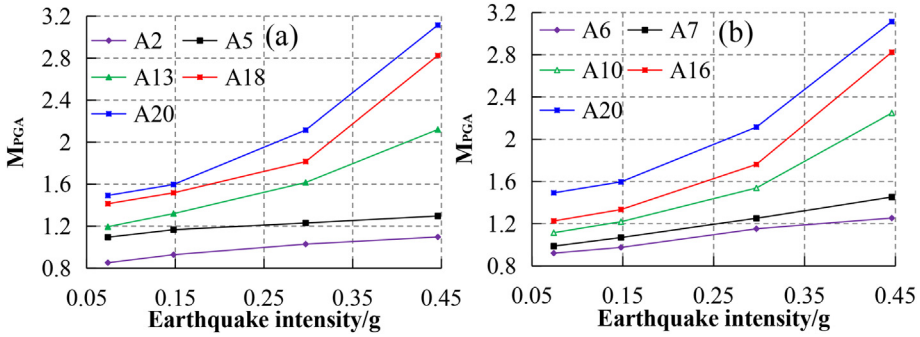

Fig. 14. The M_{PGA} of the slope with different earthquake intensities before rapid water drawdown: (a) the inside of the slope body; (b) near the slope surface.

infiltrates into the topmost structural surface and softens its material, promoting the formation, development and connection of cracks, with the slip surface forming gradually. Third, the bedding and toppling structural surfaces jointly control the failure mode of the slope. Fig. 20 shows that cracks appear in the toppling structural surfaces, providing favorable conditions for water infiltration and damage of the topmost bedding structural surface. The slope was divided into blocks by discontinuous structural surfaces, and independent blocks formed in the surface slope during earthquakes. During the formation of the landslide, the topmost bedding structural surface gradually forms the slip surface, and the toppling structural surfaces control the damage deformation characteristics of the surface slope. When the earthquake load reaches 0.446 g, the surface slope will undergo block sliding along the slip surface.

In addition, the failure mechanism of the landslide can be described as follows. First, the discontinuous structural surfaces weaken the slope stability, destroy the integrity of the slope and provide favorable conditions for the formation of separate blocks and slip surface during earthquakes. Second, the earthquakes directly induced the occurrence of cracks due to uneven movement between the blocks. Third, the rapid drawdown and water infiltration further weaken the slope stability during the earthquakes, and their effects were as follows: Fig. 21d shows that the seepage line is mainly along the first structural plane, suggesting that the water seeps into the cracks in the surface slope and softens the materials of the discontinuous structural planes in the surface slope. The discontinuous structural surfaces reach saturation rapidly, resulting in a rapid decrease in their intensities and the extension of the cracks. Moreover, the rapid drawdown results in the increase in the sliding force and the decrease in the sliding resistance in the surface slope. The rapid drawdown mainly furthers the damage deformation between the high and low water levels, as shown in Fig. 21c.

In conclusion, according to the analysis of the dynamic stability of the slope, more attention should be paid to some problems that may arise for the proposed Jinshajiang bridge. The bridge piers are critical in

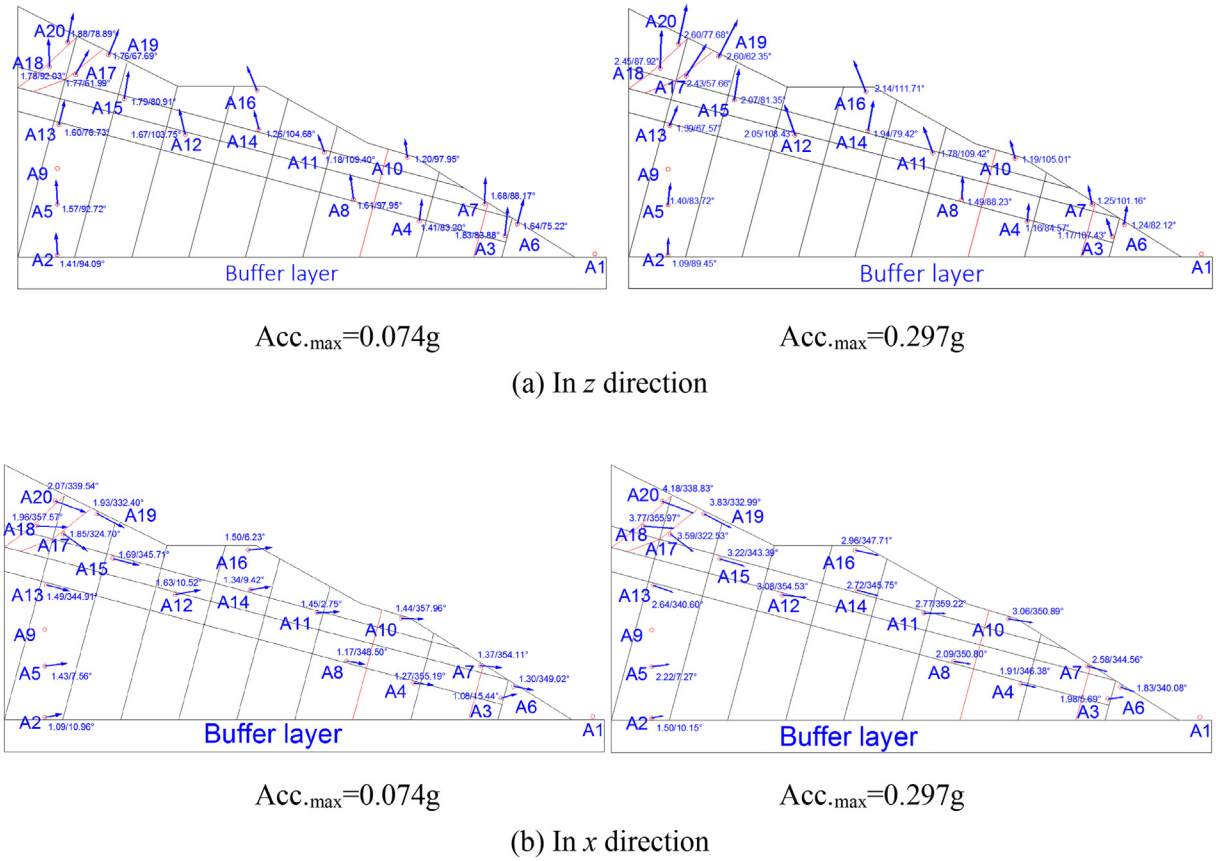

Fig. 15. Distribution of acceleration vectors under high water level: (a) in *z* direction; (b) in *x* direction.

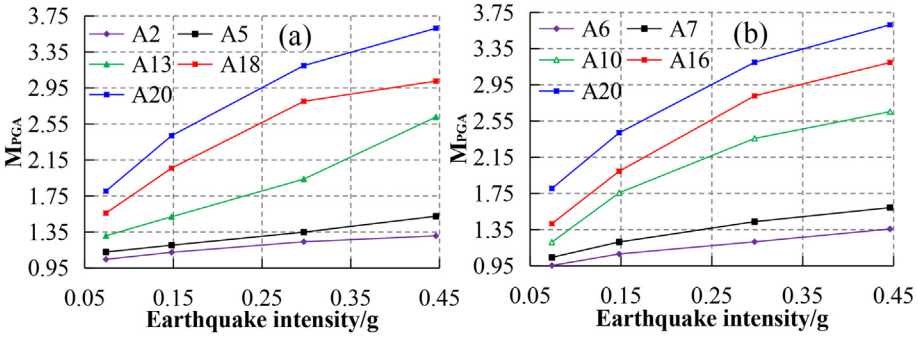

Fig. 16. The M_{PGA} of the slope with different earthquake intensities after rapid water drawdown: (a) the inside of the slope body; (b) near the slope surface.

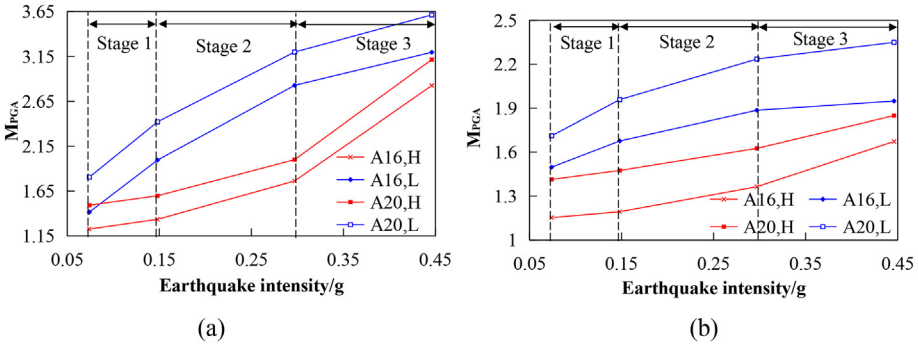

Fig. 17. M_{PGA} change rule with increasing seismic intensity for (a) input in *x* direction, and (b) input in *z* direction. H and L represent high and low water levels, respectively.

Table 4
The M_{PGAmax} of the slope when input in *x* directions.

Earthquake intensity (g)	0.074	0.148	0.297	0.446
$M_{PGAHmax}$	1.48	1.59	1.97	3.12
$M_{PGALmax}$	1.81	2.47	3.32	3.65

the actual engineering design, and their stability should be monitored. The acceleration amplification effect of the top slope and the platform is much larger than those in other areas. Discontinuous structural surfaces have an adverse effect on the slope stability. The bridge pier is located in the platform area, and the topmost bedding structural surface is the potential slip surface. Moreover, rapid drawdown also promotes the deformation of a surface slope between high and low water levels. Given the abovementioned analysis, to avoid damage during earthquakes, the bridge pier should be reinforced before completion of the bridge.

6. Conclusions

A series of shaking table tests were performed to study the dynamic stability of a rock slope with discontinuities under rapid drawdown. Some conclusions are as follows:

1. A wave absorber was installed at the end of the experimental tank to eliminate the adverse effects of water waves during earthquakes. The porous sponge and iron gauze were used to absorb the S- and P-waves, respectively. The elevation, slope surface, and surface microtopography create an amplification effect on the slope during earthquakes. M_{PGA} increases with the elevation and reaches its maximum at the top of the slope. A great change in the gradient at the slope surface results in an acceleration amplification effect near the platform. M_{PGA} of the surface slope is much larger than that of the internal slope, and the surface slope is the main amplification area. Moreover, a bedding structural surface has an impact on the amplification effect of the slope. M_{PGA} increases linearly below the bedding structural surface but undergoes a sudden increase above the structural surface.
2. The peak acceleration of the input wave mainly has an impact on the amplification effect of the slope, particularly the surface slope. Based on the observed test phenomena and the analysis of M_{PGA}, the evolution process of the damage deformation of the reservoir slope during earthquakes can be divided into three stages: formation of tiny cracks (0.074–0.148 g), crack propagation in the surface slope (0.148–0.297 g), and sliding failure (0.297–0.446 g). These stages can be analyzed more clearly by using M_{PGAH}, in particular, when larger deformation occurs, a rapid increase in M_{PGAH} can reflect the deformation more clearly than M_{PGAL} can.
3. Rapid water drawdown has a great amplification effect on the surface slope during earthquakes and further promotes the deformation of the surface slope, particularly between the high and low water levels. M_{PGA} after rapid drawdown is approximately 1.2–1.5 times that before rapid drawdown during earthquakes. S-waves have a greater impact on the amplification effect than that of P-waves under the combined action of rapid drawdown and earthquakes. Rapid drawdown has a great impact on the amplification effect of the slope from 0.148 to 0.297 g, but the amplification effect began to reduce after the occurrence of failure deformation from 0.297 to 0.446 g. The 0.148–0.297 g stage is the cumulative deformation failure stage, and 0.297 g is the critical failure state of the slope. When ΔM_{PGA} is > 0.65, under rapid drawdown and earthquakes, the surface slope enters the failure stage from the plastic stage.
4. According to the acceleration vectors of the blocks, the differences in the acceleration vectors between the adjacent blocks were the main trigger of the slope deformation during earthquakes. The P-waves mainly induced the uneven settlement deformation of blocks under the vertical earthquake load, while the S-waves mainly induced the horizontal sliding movement of the surface slope under the horizontal seismic load. In particular, S-waves have a dominant

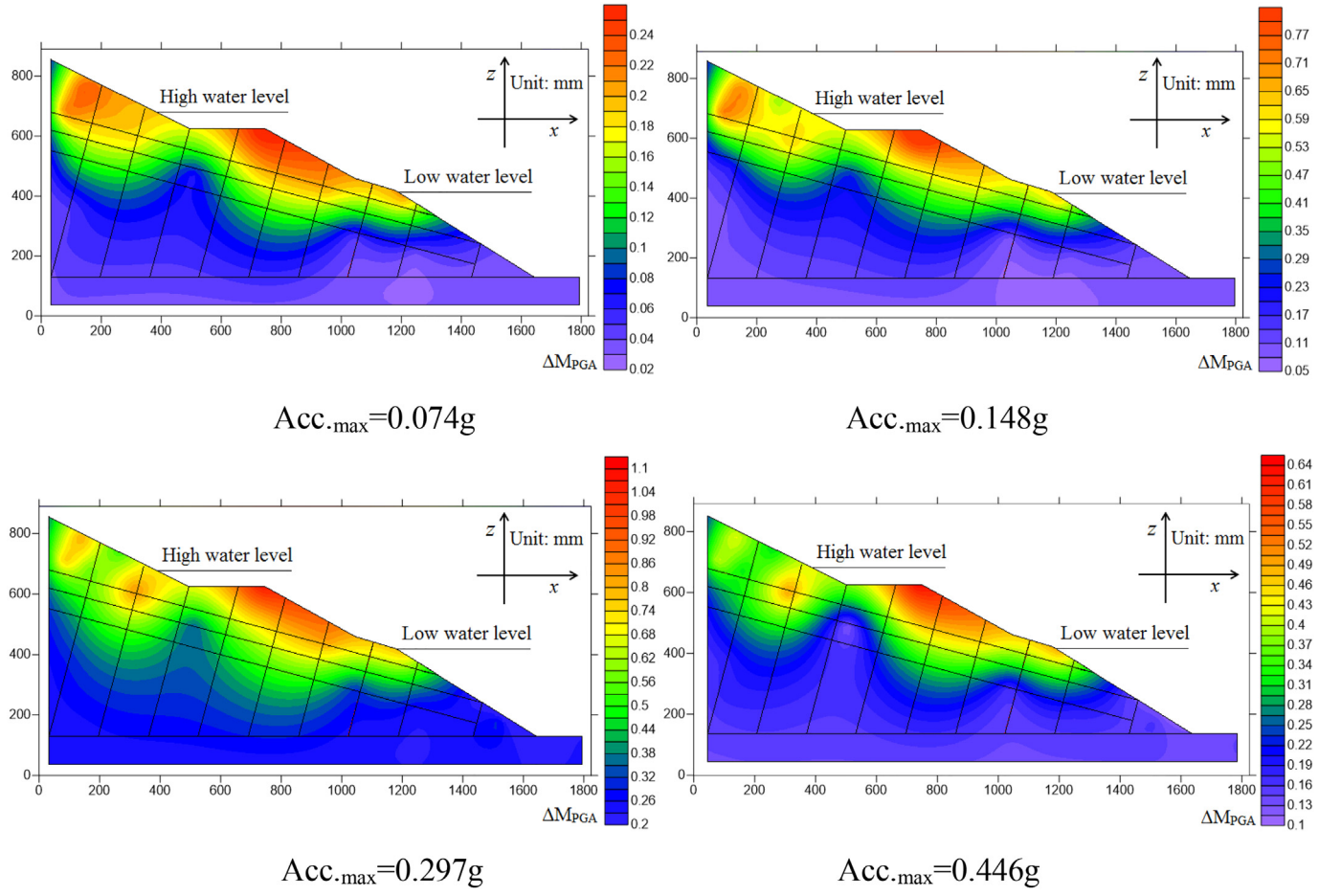

Fig. 18. Distribution of ΔM_{PGA} after rapid drawdown when input in *x* direction.

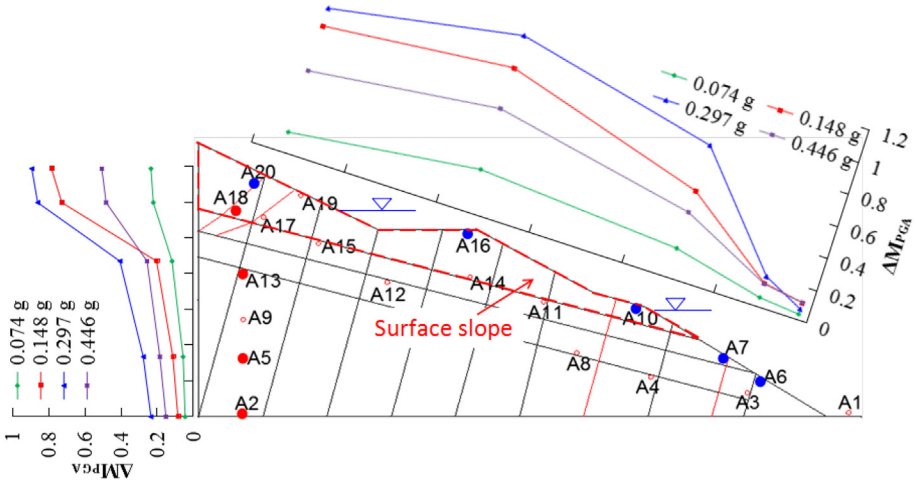

Fig. 19. ΔM_{PGA} of the slope under rapid drawdown when input in *x* direction.

effect on the slope deformation. Additionally, the weak structural surfaces are closely related to the slope damage characteristics. The bedding structural surfaces have a dominant effect on the failure mode, and the effects mainly include three aspects: First, the toppling structural surface controls the formation and development of cracks. Second, the bedding structural surface controls the formation of the slip surface. Third, the bedding and toppling structural surfaces control the failure mode. The surface slope will slide along the topmost structural plane in the form of blocks under rapid drawdown and earthquakes.

Acknowledgments

This work is supported by the National Natural Science Foundation of China (No. 11372180), National Key R & D Program of China, China (2018YFC0809400). The authors would like to express their gratitude to Zhijian Wu of Key Laboratory of Loess Earthquake Engineering, CEA Gansu Province for their helpful advice.

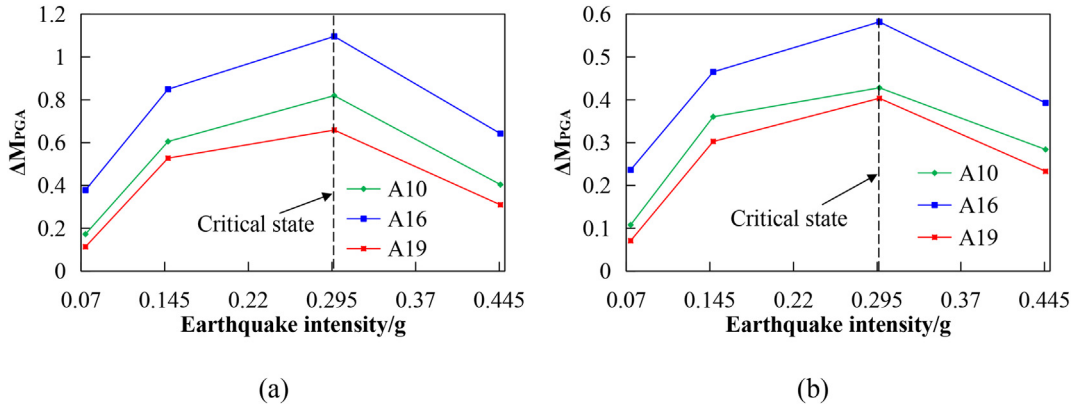

Fig. 20. ΔM_{PGA} change rule with increasing seismic intensity for (a) input in *x* direction, and (b) input in *z* direction.

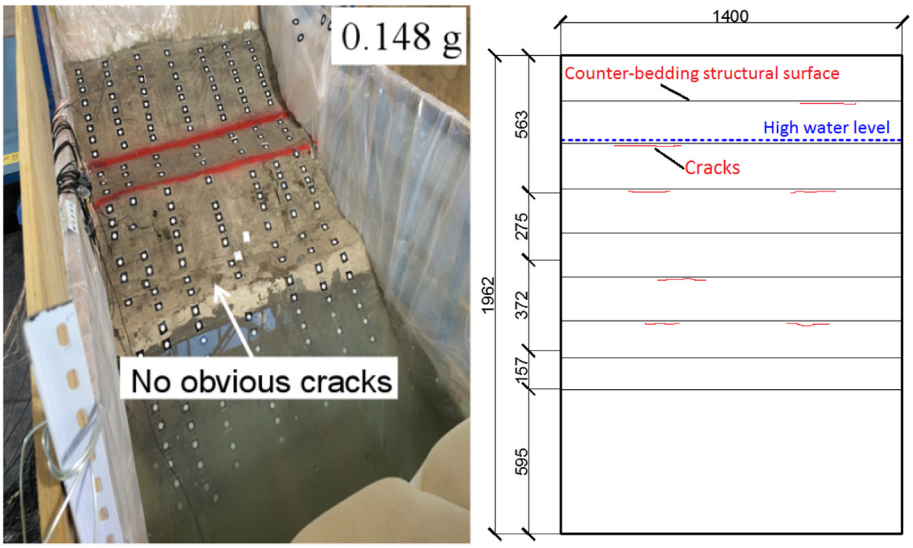

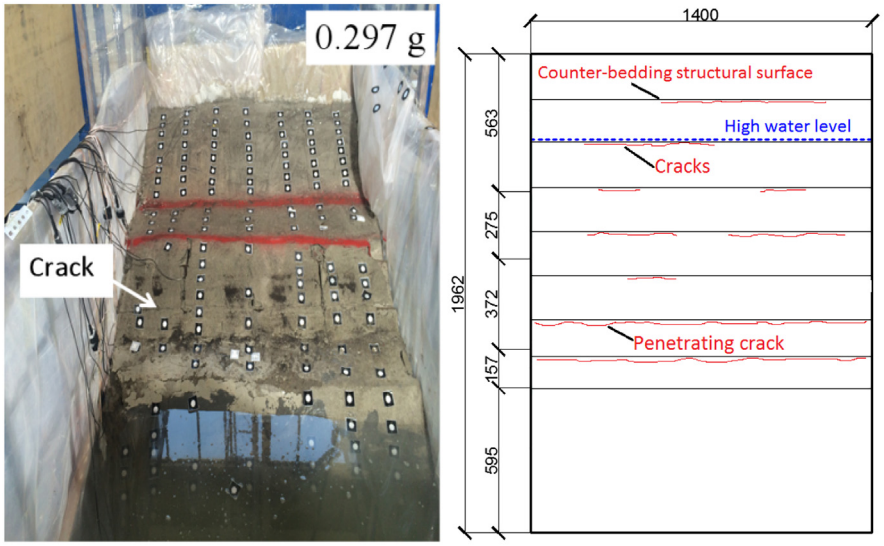

Fig. 21. Failure process of the slope: (a) 0.148 g; (b) 0.297 g; (c) 0.446 g; (d) Deformation characteristics of the slope (Unit: mm).

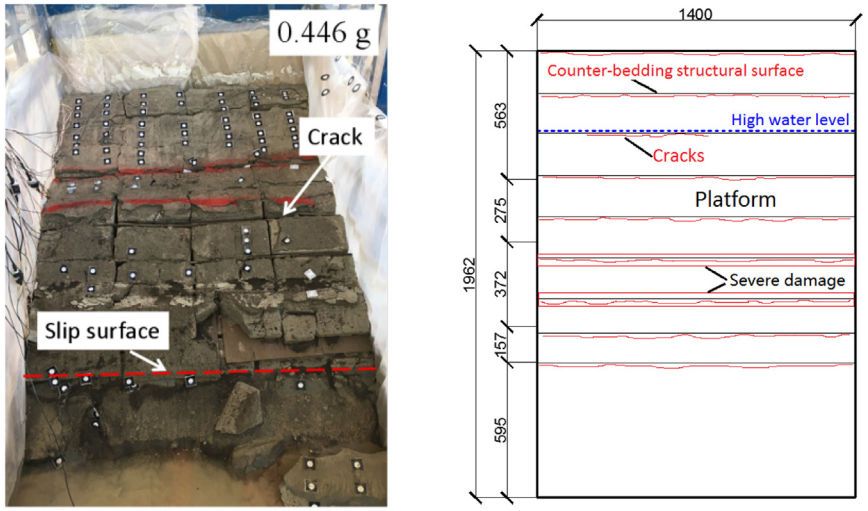

(c)

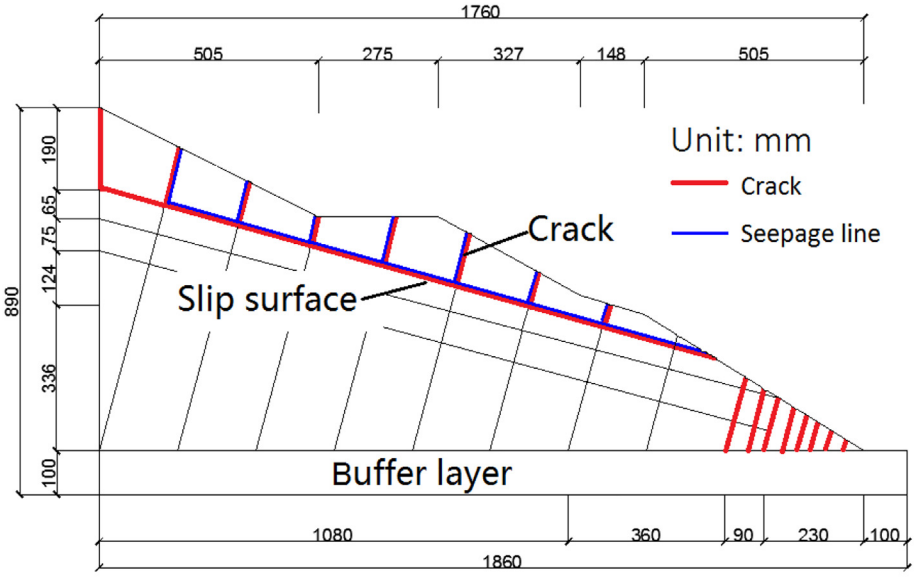

(d)

Fig. 21. (*continued*)

References

Berilgen, M.M., 2007. Investigation of stability of slopes under water drawdown conditions. Comput. Geotech. 34 (2), 81–91.

Che, A.L., Yang, H.K., Wang, B., Ge, X.R., 2016. Wave propagations through jointed rock masses and their effects on the stability of slopes. Eng. Geol. 201, 45–56.

Chen, Z.L., Hu, X., Xu, Q., 2016. Experimental study of motion characteristics of rock slopes with weak intercalation under seismic excitation. J. Mt. Sci. 13 (3), 546–556.

Dai, F.C., Xu, C., Yao, X., Xu, L., Tu, X.B., Gong, Q.M., 2011. Spatial distribution of landslides triggered by the 2008 ms 8.0 Wenchuan earthquake, china. J. Asian Earth Sci. 40 (4), 883–895.

Dong, H.K., Gratchev, I., Balasubramaniam, A., 2015. Back analysis of a natural jointed rock slope based on the photogrammetry method. Landslides 12 (1), 147–154.

Fan, G., Zhang, J., Wu, J., Yan, K., 2016. Dynamic response and dynamic failure mode of a weak intercalated rock slope using a shaking table. Rock Mech. Rock. Eng. 49 (8), 1–14.

Gao, Y.F., Zhu, D.S., Lei, G.H., Qin, H.Y., 2014. Stability analysis of three-dimensional slopes under water drawdown conditions. Can. Geotech. J. 51 (6), 1355–1364.

Geli, L., Bard, P.Y., Jullien, B., 1988. The effect of topography on earthquake ground motion: a review and new results. Bull. Seismol. Soc. Am. 78 (1), 42–63.

Ghiassi, K., 1998. Failure Modes of Asperities in Rock Discontinuities (Doctoral dissertation). University of Illinois at Urbana-Champaign.

Gischig, V.S., Eberhardt, E., Moore, J.R., Hungr, O., 2015. On the seismic response of deep-seated rock slope instabilities — insights from numerical modeling. Eng. Geol. 193, 1–18.

Goodman, R.E., 1989. Introduction to Rock Mechanics, second ed. Wiley, New York.

Gyongy, I., Richon, J.B., Bruce, T., Bryden, I., 2014. Validation of a hydrodynamic model for a curved, multi-paddle wave tank. Appl. Ocean Res. 44 (44), 39–52.

Huang, R., Zhao, J., Ju, N., Li, G., Min, L.L., Li, Y., 2013. Analysis of an anti-dip landslide triggered by the 2008 Wenchuan earthquake in china. Nat. Hazards 68 (2), 1021–1039.

Huang, D., Cen, D., Ma, G., Huang, R., 2015. Step-path failure of rock slopes with intermittent joints. Landslides 12 (5), 911–926.

Jiang, T., Liu, Y., Ma, Jin, 2013. Time history response analysis of jointed rock slope under seismic loads. Chin. J. Rock Mech. Eng. 32, 3938–3944.

Lee, C.C., 2001. Reflection and transmission phenomena of waves propagating between an isotropic medium and an arbitrarily oriented anisotropic medium. Opt. Lett. 26 (4), 190–192.

Li, Y., Chen, X.Z., Chen, L.J., Guo, X.Y., 2015. Investigation on the rupture process of the Ludian MS 6.5 earthquake sequence on 3 August, 2014 in Yunnan province. Chin. J. Geophys. 58 (9), 3232–3238.

Lin, M.L., Wang, K.L., 2006. Seismic slope behavior in a large-scale shaking table model test. Eng. Geol. 86 (2–3), 118–133.

Lin, Y.L., Leng, W.M., Yang, G.L., Li, L., Yang, J.S., 2015. Seismic response of embankment slopes with different reinforcing measures in shaking table tests. Nat. Hazards 76 (2), 791–810.

Liu, H.X., Xu, Q., Li, Y.R., Fan, X.M., 2013. Response of high-strength rock slope to seismic waves in a shaking table test. Bull. Seismol. Soc. Am. 103, 3012–3025.

Liu, Y., Li, H., Xiao, K., Li, J., Xia, X., Liu, B., 2014. Seismic stability analysis of a layered

rock slope. Comput. Geotech. 55 (1), 474–481.
Moregenstern, N., 2015. Stability charts for earth slopes during rapid drawdown. Géotechnique 13 (2), 121–131.
Shao, W., Bogaard, T., Bakker, M., Berti, M., 2016. The influence of preferential flow on pressure propagation and landslide triggering of the rocca pitigliana landslide. J. Hydrol. 543, 360–372.
Song, D.Q., Che, A., Zhu, R.J., Ge, X.R., 2017a. Dynamic response characteristics of a rock slope with discontinuous joints under the combined action of earthquakes and rapid water drawdown. Landslides 1–17.
Song, D.Q., Feng, X.B., Wang, Z.Q., Song, H.Q., 2017b. Using near-real-time monitoring of landslide deformation to interpret hydrological triggers in Jiudian Gorge reservoir. Indian J. Geo-Marine Sci. 46 (11), 2182–2190.
Twu, S.W., Lin, D.T., 1991. On a highly effective wave absorber. Coast. Eng. 15 (4), 389–405.
Twu, S.W., Wang, Y.T., 1994. A computational model of the wave absorption by the multilayer porous media. Coast. Eng. 24 (1–2), 97–109.
Wang, K.L., Lin, M.L., 2011. Initiation and displacement of landslide induced by earthquake — a study of shaking table model slope test. Eng. Geol. 122 (1–2), 106–114.
Wang, F., Cheng, Q., Highland, L., Miyajima, M., Wang, H., Yan, C., 2009. Preliminary investigation of some large landslides triggered by the 2008 Wenchuan earthquake, Sichuan province, china. Landslides 6 (1), 47–54.
Wasowski, J., Keefer, D.K., Lee, C.T., 2011. Toward the next generation of research on earthquake-induced landslides: current issues and future challenges. Eng. Geol. 122, 1–8.
Xia, M., Ren, G.M., Ma, X., 2013. Deformation and mechanism of landslide influenced by the effects of reservoir water and rainfall, three gorges, china. Nat. Hazards 68 (2), 467–482.
Xu, B.T., Yan, C.H., 2014. An experimental study of the mechanical behavior of a weak intercalated layer. Rock Mech. Rock. Eng. 47 (2), 791–798.
Yang, J., Zeng, Z., Li, M., et al., 2015. The seismo-geological hazards and seismogenic structure of the 2013 Deqing-derong 5.9 earthquake. Earth Sci. 40 (10), 1701–1709.
Yin, Y., 2008. Researches on the geo-hazards triggered by Wenchuan earthquake, Sichuan. J. Eng. Geol. 16 (4), 433–444.
Zhan, J.M., Dong, Z., Han, Y., Jiang, W., 2010. Numerical simulation of wave transformation incorporating porous media wave absorber. J. Hydrodyn. Ser. B 22 (5), 982–985.
Zhou, J.W., Jiao, M.Y., Xing, H.G., Yang, X.G., Yang, Y.C., 2017. A reliability analysis method for rock slope controlled by weak structural surface. Geosci. J. 21 (3), 453–467.
Zhu, S., Chwang, A.T., 2001. Analytical study of porous wave absorber. J. Eng. Mech. 127 (4), 326–332.